Marine Georesources & Geotechnology

ISSN: (Print) (Online) Journal homepage: https://www.tandfonline.com/loi/umgt20

Bearing performance of steel pipe pile in multilayered marine soil using fiber optic technique: A case study

Sheng-Hua Xu, Zheng-Wu Li, Yong-Feng Deng, Xia Bian, Hong-Hu Zhu, Feng Zhou & Qi Feng

MARINE GEORESOURCES & GEOTECHNOLOGY
https://doi.org/10.1080/1064119X.2021.2005192

Bearing performance of steel pipe pile in multilayered marine soil using fiber optic technique: A case study

Sheng-Hua Xu[a], Zheng-Wu Li[b], Yong-Feng Deng[a], Xia Bian[c], Hong-Hu Zhu[d], Feng Zhou[e] and Qi Feng[e]

[a]Institute of Geotechnical Engineering, School of Transportation, Southeast University, Nanjing, China; [b]Lianyungang Xinxugang Hydrocarbon Terminal Co., Ltd., Lianyungang, China; [c]Key Laboratory of Ministry of Education for Geomechanics and Embankment Engineering, Hohai University, Nanjing, China; [d]School of Earth Science and Engineering, Nanjing University, Nanjing, China; [e]School of Transportation, Nanjing University of Technology, Nanjing, China

ABSTRACT
It is important to appraise the performance of the steel pipe pile performance in harbor engineering. The load transfer mechanism and pile-soil interaction could not be clearly understood using the traditional measurement. In this case, fiber Bragg grating (FBG) and Brillouin optical time domain reflectometry (BOTDR) were applied simultaneously at an open-ended steel pipe pile field test in Ganyu Port, China. Results showed that the fiber optic sensing system accurately measured the axial force, side friction, and bearing behaviors of open-ended steel pipe piles based on strain data. During the pile driving stage, the system captured the bending deformation and eccentric load on the upper part of the pile above the mud surface, identifying the relatively large tensile strain at the final stage of driving. For the static load test, the strain and resistance distribution obtained by sensing systems suggested that 80% of pile compression was concentrated in the upper 20 m, and the maximum force was observed at the location of soil surface. The precision of high strain dynamic tests is limited for complex field conditions and model's parameters-setting.

ARTICLE HISTORY
Received 13 May 2021
Accepted 15 September 2021

KEYWORDS
Open-ended steel pipe piles; dynamic driving process; bearing performance; static load test; high strain dynamic test; fiber optic sensing

1. Introduction

The large-diameter steel pipe pile has been used extensively in offshore platform foundations of bridges, piers, wind farms and deep-water ports, due to its high load-bearing capacity, light weight, relatively low cost, and outstanding penetration performance (Han et al. 2017; Li et al. 2019; Sun et al. 2016; Bian et al. 2021). During the construction of coastal infrastructure platforms, field tests were required to evaluate the performance of large-diameter steel pipe piles, especially dealing with the marine soil with complex geology condition, to ensure the stability of the foundation. In the pile test, various sensors were usually pasted on the surface to monitor the stress and strain along the pile body dynamically and statically, to determine the pile-soil interaction and the pile bearing capacity. Commonly, the traditional sensors were subjected to easy rust damage, insufficient data representation, and severe electromagnetic interference. In addition, these kinds of apparatuses, including vibrating-wire sensors and resistance strain sensors, are based on the point (discrete) monitoring method, which can only provide limited data at specific positions. This would make it more difficult to precisely caputure the pile-soil interaction in the multilayer marine strata and to meet the design requirements of some projects. On the contrary, the distributed and quasi-distributed optical fiber techniques have become one of the important means of civil engineering infrastructure monitoring, especially pile foundation testing, because of its low loss, high sensitivity, anti-interference, convenient installation, and continuous measurement (Barrias, Casas, and Villalba 2016; Doherty et al. 2015; Fattah, Zbar, and Mustafa 2017; Mohamad, Soga, and Amatya 2014; Van Ravenzwaaij et al. 2018; Webb et al. 2017).

In this paper, a field pile testing in Ganyu port district, Lianyungang Port, Jiangsu Province of China was reported. Brillouin optical time domain reflectometry (BOTDR) and fiber Bragg grating (FBG) sensing techniques were integrated to monitor the pile driving process, full-scale axial compression, and uplift static loading test of two steel pipe test piles.

The primary objectives of this study are: (1) to correlate the two methods of high strain dynamic tests and static load tests in ascertaining the vertical ultimate bearing capacity, tip resistance, side friction, and its distribution along the test pile; (2) to validate the effectiveness of optic fiber sensing techniques including FBG and BOTDR in comparison with conventional dynamic loading tests for determining load transfer behaviors of pile shaft; and (3) to evaluate the performance of impact system and the preset bearing stratum.

2. Fiber optic sensing techniques

In this paper, BOTDR and FBG sensing techniques based on different principles were mainly used to measure the axial stress distribution of the pile during the static and

CONTACT Yong-Feng Deng noden@seu.edu.cn

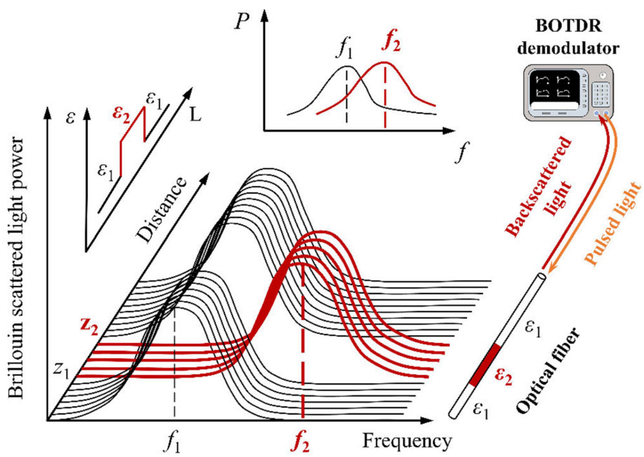

Figure 1. BOTDR strain measurement mechanism.

dynamic processes instead of traditional strain gauges. The reason for the joint application of these two methods is that BOTDR has the shortcoming of relatively low resolution, which is limited to measure the full-distance distributed strain along the steel pipe pile. FBG sensing method is then integrated into BOTDR as compensation for higher-precision strain detection of critical sections.

The principles and installation of these two fiber optic sensing systems are briefly introduced as follows.

2.1. Principle of BOTDR

Optical fiber has a long history as a tool of signal transmission. Brillouin optical time domain reflectometry (BOTDR) is a kind of distributed fiber optic sensing (DFOS) technology that extends the ordinary optical fibers with functions for sensing as well. Relying on the sensing optical cable, it can monitor strain across the entire length of the pile with a spatial resolution of 1 m and a pulse width of 10 ns.

A narrow bandwidth Distributed Feedback (DFB) pulsed light with a specific frequency is launched into an optical fiber, generating the nonlinear interaction between the incident light and thermally excited acoustic phonons. Various scattering phenomena occur to this interaction, and one of them is spontaneous Brillouin backscattered signals at different positions, which propagate back to the input end and are detected by the heterodyne coherency system in the time domain. This Brillouin scattering spectrum could be affected by both temperature and strain within the propagation medium, that is, the frequency of the backscattered light will shift linearly with strain and temperature changes along the optical fiber (Lu et al. 2012).

According to the temperature, time, and frequency shift signals monitored by the attached sensing optical cable and the demodulator, the strain distribution along the whole steel pipe pile can be determined by Equations (1) and (2). The schematic diagram of BOTDR measurement is shown in Figure 1.

The linear relationship between Brillouin frequency shift $\upsilon_B(\varepsilon, T)$ and optical fiber temperature T and strain ε can be expressed as:

$$\upsilon_B(\varepsilon, T) = \upsilon_B(0, T_0) + \frac{\partial \upsilon_B(\varepsilon)}{\partial \varepsilon}\varepsilon + \frac{\partial \upsilon_B(T)}{\partial T}(T - T_0) \qquad (1)$$

where $\upsilon_B(0,\ T_0)$ is approximately 11.0 GHz, representing the frequency shift with the initial temperature T_0 and no strain; $\frac{\partial \upsilon_B(\varepsilon)}{\partial \varepsilon}$ and $\frac{\partial \upsilon_B(T)}{\partial T}$ represent the proportional coefficients of strain and temperature, respectively, which are constant after consignment (Campanella et al. 2018; Shi et al. 2003).

The light transmission distance Z, which actually is the specific position of generated strain change to the input end, is determined by time-domain analysis. The distance Z can be determined as:

$$Z = \frac{ct}{2n} \qquad (2)$$

where c is the velocity of light in vacuum; t is the time interval between the incident light and the backscattered light at the input end, and n is the refractive index of the optical fiber.

2.2. Principle of FBG

Fiber Bragg grating (FBG) is a kind of quasi-distributed fiber optic strain measurement method. Generally, the fiber gratings are encapsulated as different types of fiber grating sensors, attached along the test pile regularly. The advantages of FBG strain sensors include lightness, durability, high accuracy (up to 1 $\mu\varepsilon$), and dynamic real-time detection (Lee et al. 2004; Wu et al. 2016; Yi 2016).

The Bragg grating is manufactured with micro-fabrication methods in the periodic or aperiodic permanent modulation of the refractive index of the fiber core along the fiber axis, forming a spatial phase structure in the fiber core. Therefore, the wavelength is an inherent parameter of one fiber Bragg grating.

The Bragg grating wavelength, λ_B (nm), is defined by:

$$\lambda_B = 2n_{eff}\Lambda \qquad (3)$$

where n_{eff} is the effective refractive index; Λ is the grating pitch.

During the test pile detection procedure, an Amplified Spontaneous Emission (ASE) broadband light is employed as the sensing source. If the wavelength of incident light matches the specific Bragg phase condition of one sensor, then the reflected light occurs and will be detected. Otherwise, the light will transmit along the fiber continually.

The initial wavelength λ_B of one FBG sensor is constant in normal temperature and stress-free condition. When the photoelectric monitor system detects the wavelength change $\Delta\lambda$ of the FBG sensor closely fitted with the test pile, it indicates the change of stress or temperature in this position. The wavelength-change rate of the fiber Bragg grating always varies linearly with the changes of temperature and axial stress. Therefore, by monitoring the wavelength change in real time, the changes of temperature and strain can be calculated. According to the principle of wavelength division multiplexing, several FBG sensors with different initial wavelengths could be installed along the test pile at certain intervals and connected in series, which can accurately measure

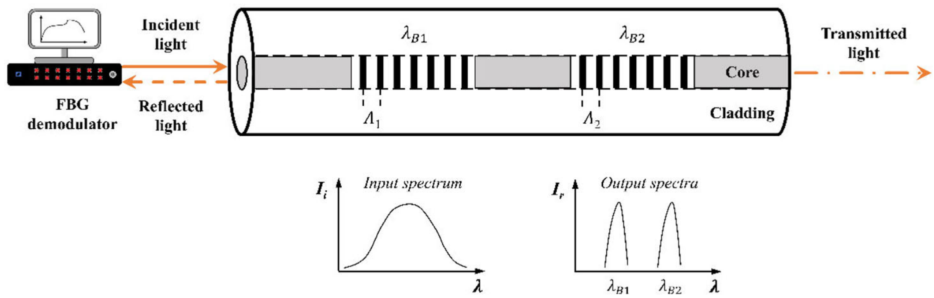

Figure 2. Working principle and multiplexing of FBG sensors.

the strain change of key sections during the pile testing. The working principle of FBG strain sensors is shown in Figure 2.

According to the coupled mode theory, when the phase matching condition is satisfied, the resonant wavelength of the grating is shown as:

$$\frac{\Delta\lambda}{\lambda_B} = \eta\varepsilon + \gamma(T - T_0) \tag{4}$$

where $\frac{\Delta\lambda}{\lambda_B}$ is the wavelength change rate of the grating; η and γ represent the strain and temperature coefficient respectively which are constant; ε is the axial strain of fiber; and $(T - T_0)$ is the temperature change.

2.3. Installation of sensing systems

In this study, the BOTDR sensing optical cable, FBG strain sensors and temperature sensors were attached on the pile surface, leaving no space. It ensures that sensors and the test pile could deform synchronously to achieve better signal transmission and more precise data acquisition. FBG sensors were connected in series by 0.9 mm strain sensing optical fiber. The BOTDR standard single-mode optical fiber was embedded in carbon fiber cloth to improve the data accuracy and defense capability. The installation procedures of the fiber optic sensing systems to the steel pipe pile are presented below and shown in Figure 3.

1. ***GRIND***: According to the layout of sensors on the pile shaft in the design, the surface at corresponding positions was polished with a grinder removing the rust. All raised welds on the external surface of the pile along the laying route were ground flat and smooth to prevent light loss and detection error. Each ground position was then cleaned with alcohol.
2. ***PASTE***: FBG strain sensors were coated with thermal conductive silica gel, then welded on the pile surface with a spot welder and connected in series through 0.9 mm strain sensing optical fiber to form a loop. FBG temperature sensors were connected in series by relay fiber and glued to the pile surface. The BOTDR carbon fiber composite strain test strip was covered on the FBG test routes and pasted on the pile surface with glue.
3. ***PROTECT***: After the glue solidified, the BOTDR carbon fiber strip was completely covered with aluminum foil tape as the heat insulation protective layer. To prevent the damage of optical fibers during pile driving, a steel channel was welded above the monitoring routes. The exposed part of all fibers near the pile top was protected with rigid steel wire plastic tubes.

To prevent data loss caused by optical fiber damage during the field tests, two groups of fiber optic monitoring routes with identical configuration were symmetrically arranged on both sides of the test pile, named as "Side A" and "Side B". For a single test pile, each monitoring route contained a set of FBG strain test loops, an FBG temperature test optical fiber and a set of BOTDR strain sensing loops. Furthermore, each FBG strain test loop consisted of 9 strain sensors in series and the FBG temperature test optical fiber consisted of 5 temperature sensors in series. The configuration scheme of the fiber optic monitoring route on one side of any test pile is shown in Figure 4.

In this study, the cabinet type modular fiber grating demodulator developed by Suzhou NanZee Sensing Technology Co., Ltd. was selected as the main measurement device of FBG sensing data (Zheng et al. 2021; Zhu, Shi, and Zhang 2017). This demodulator can calculate the center wavelength of FBG sensor by changing the output wavelength of tunable light source. The BOTDR measurement device is developed by 41st Institute of China Electronics Technology Co., Ltd. (CETC 41st). The technical parameters of these demodulators are shown in Table 1.

Moreover, the FBG patch strain sensors, temperature sensors, and BOTDR carbon fiber composite strain sensing cable used in this study were developed by Suzhou NanZee Sensing Technology Co., Ltd.

3. Project overviews

A designed wharf for a 50,000 GT liquefied hydrocarbon berth and its ancillary structures were located in Ganyu Port District, Lianyungang Port, Lianyungang City, Jiangsu Province of China. The location of the pile test is shown in Figure 5. According to the design, the wharf adopted a high pile beam slab structure, and the pile foundation type was mainly selected as open-ended steel pipe piles with diameter of 800 mm. Since there was no analogous pile driving experience and static loading test data in this port, the pile testing must be implemented to verify the design and to provide a reliable basis for the further construction of the wharf. Figure 6 shows the layout of various piles required

Figure 3. The installation procedure: (a) GRIND, (b) PASTE, (c, d) PROTECT.

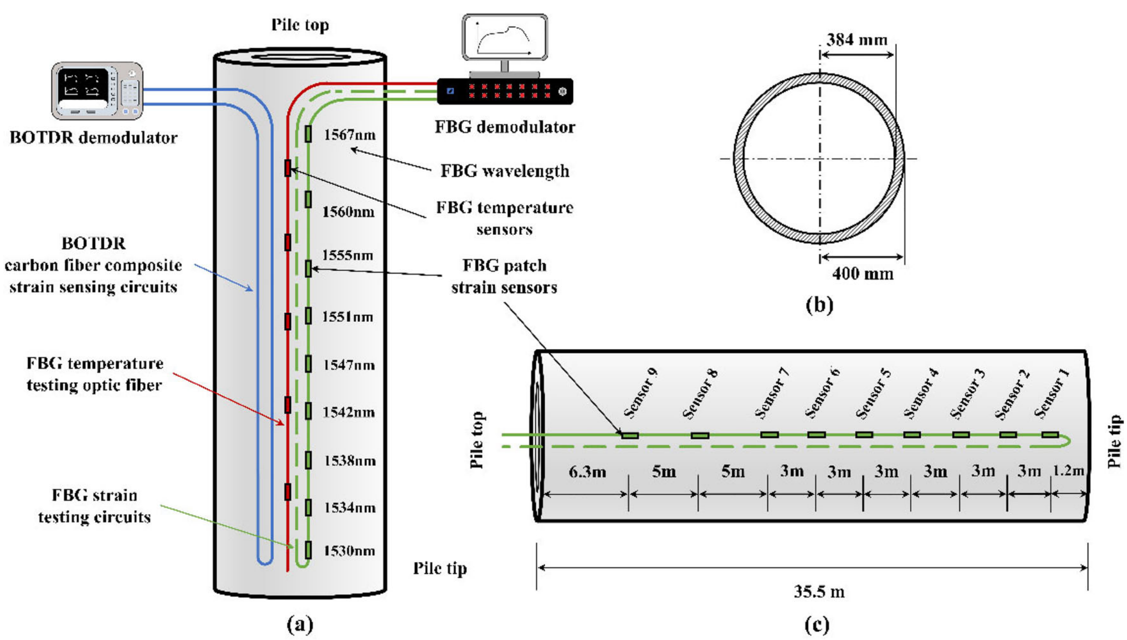

Figure 4. Configuration diagram of fiber optic monitoring route of T1 "Side A": (a) general scheme; (b) cross section dimension; (c) layout of FBG strain sensors.

Table 1. Technical parameters of two fiber optic demodulators.

Demodulator	Model	Wavelength (nm)	Strain resolution (microstrain)
FBG	NZS-FBG-A01 (C)	1527–1568	1
BOTDR	AV6419	1545–1555	50

for the field pile test and the front view of them after installation.

High strain dynamic test and axial compression static load test were carried out for test piles T1 and T2. However, the axial uplift static load test was only carried out for pile T1. The steel pipe piles, including test piles and anchor piles, conformed to the material and dimensional requirements of ASTM A252/A252M −19, Grade 3 steel were painted by epoxy anti-corrosion coating within 1 ∼ 16 m below the pile top. The parameters of piles are listed in Table 2.

Table 3 presents the typical stratigraphy properties. The strata profile of the test field could be primarily divided into three layers: marine sedimentary layers, continental sedimentary layers and bedrock weathering layers. In this study, the strongly weathered gneiss was proposed as the bearing stratum. The local theoretical lowest tidal level was taken as the datum elevation. The bottom elevation of the strongly weathered gneiss was −30.69 m with a thickness of 3.17 m. The mud surface elevation was −5.50 m. The design embedment depth of the steel pipe pile tip was −28.50 m. As

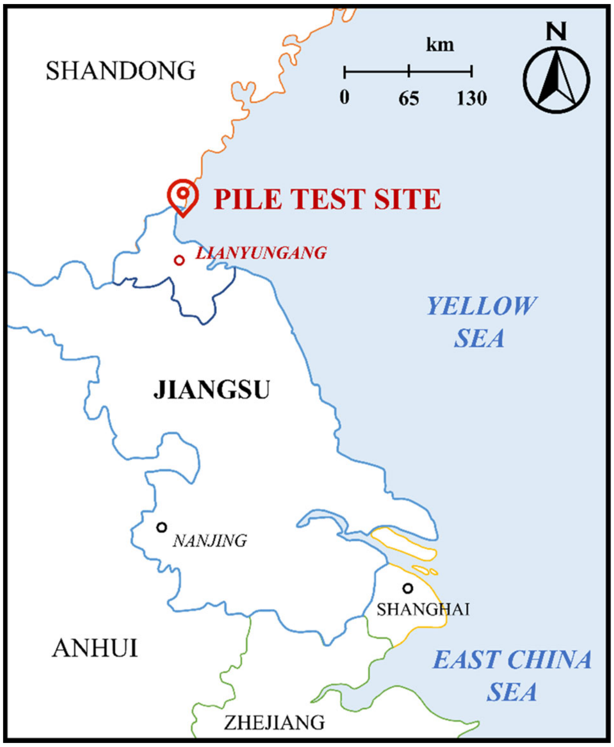

Figure 5. Location of the pile testing site.

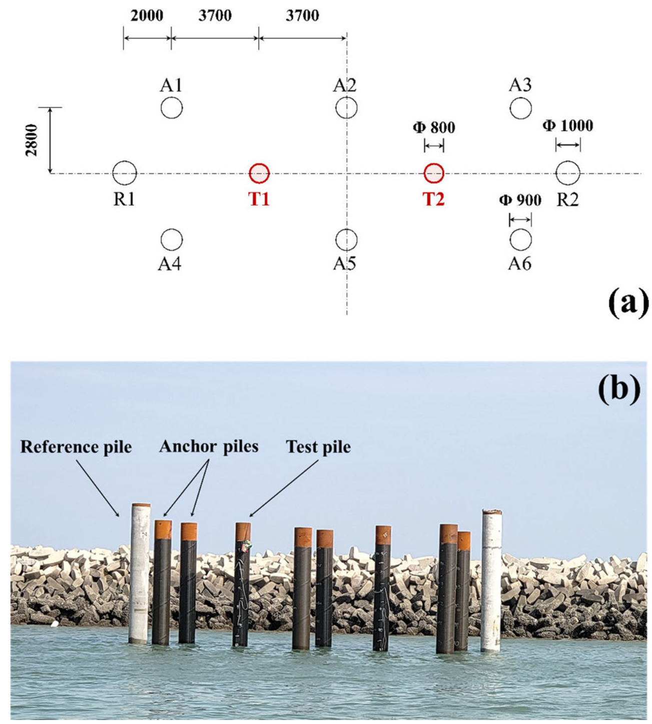

Figure 6. Diagrams of: (a) layout of various piles (A: Anchor pile; T: Test pile; R: Reference pile; unit: mm) and (b) the front view after installation.

shown in Figure 7, the actual embedment depth of pile T1 was −28.10 m, and that of pile T2 was −28.00 m.

4. Field pile test scheme

The pile test was divided into three stages as follows.

1. The open-end steel pipe piles were driven into the bearing stratum by a diesel hammer. During the pile driving process, BOTDR and FBG sensing systems simultaneously monitored the strain along the pile shaft. When the pile cap was rammed by the hammer, the time-dependent strain data were collected by corresponding demodulators. Therefore, the pile-soil interaction and load transfer mechanisms could be investigated during the driving process. Meanwhile, the strain transducers and accelerometers, installed symmetrically on both sides near the pile top, detected the strain and acceleration signals which were then saved in the pile dynamic analyzer. Accordingly, the impact force and transferred energy of the driven pile could be analyzed.
2. The high strain dynamic tests were carried out to ascertain the axial compressive bearing capacity and the integrity of test pile. A 14-day elapsed time was set between the initial strike test and restrike test, to assess the ultimate axial compressive static capacity at initial installation and after excessive pore water pressure dissipated in the perimeter of piles.
3. Axial compression and uplift static load tests were carried out after 28 days of pile installation. In the static load test, BOTDR and FBG sensing systems were used to monitor the pile strain at each load increment and decrement. Accordingly, the internal force, side friction distribution and pile tip resistance were obtained from the recordings. The ultimate axial compressive static capacity was derived from different failure criteria and compared with the results of high strain dynamic tests.

4.1. Principle and arrangement of dynamic load test

High strain dynamic test (HSDT) was performed in accordance with ASTM D4945-17 (ASTM-D4945 2017) and the test results were handled by model BETC-C6A Pile Dynamic Analyzer which is developed by China Academy of Building Research (CABR). The analyzer consists of two parts. The composition of the measuring system is shown in Figure 8. It should be noted that strain transducers and accelerometers were installed at a distance below the pile top to avoid higher distortion areas and to improve data quality.

When the diesel hammer impacts the pile top, the pile shaft was compressed, with relative displacement between pile and soil. The impact effect propagates to the pile tip in the form of stress wave, reflecting back to the pile top. A pair of strain transducers and piezoelectric accelerometers, which were mounted symmetrically on the external surface using screws, would receive the instantaneous dynamic signals generated at the installation section according to a specific frequency. The signals were then de-noised, amplified and analog to digital (A/D), converting into velocity and force-time history signals. By analyzing the signals using different methods, it is possible to understand the pile-soil interaction during and after the completion of pile driving, and to obtain relevant indices of engineering concern.

Table 2. Parameters of all kinds of piles.

Function	Type	Amount	Diameter (mm)	Length (m)
Test pile	Open-end steel pipe pile	2	800	35.5
Anchor pile	Open-end steel pipe pile	6	900	36.0
Reference pile	Prestressed Hollow Concrete pile	2	1000	36.0

Table 3. Soil profile at the test field.

Layer number	Bottom elevation (m)	Soil description	Geological time	Average $N_{63.5}$ (S.P.T.)
①$_1$	−6.92	Mud	Q_4^{m}	<1
①$_3$	−8.12	Coarse gravel sand with sludge	Q_4^{m}	4.6
②	−10.12	Medium sand	Q_4^{al+pl}	12.5
②$_1$	−12.62	Silty clay	Q_4^{al+pl}	9.5
②$_{1-1}$	−13.72	Clay	Q_4^{al+pl}	14.2
②$_2$	−16.82	Medium coarse sand	Q_4^{al+pl}	22.9
②$_3$	−19.12	Clay	Q_4^{al+pl}	17.5
②$_4$	−27.52	Coarse gravel sand	Q_4^{al+pl}	39.4
③$_2$	−30.69	Strongly weathered gneiss	P_t	>50

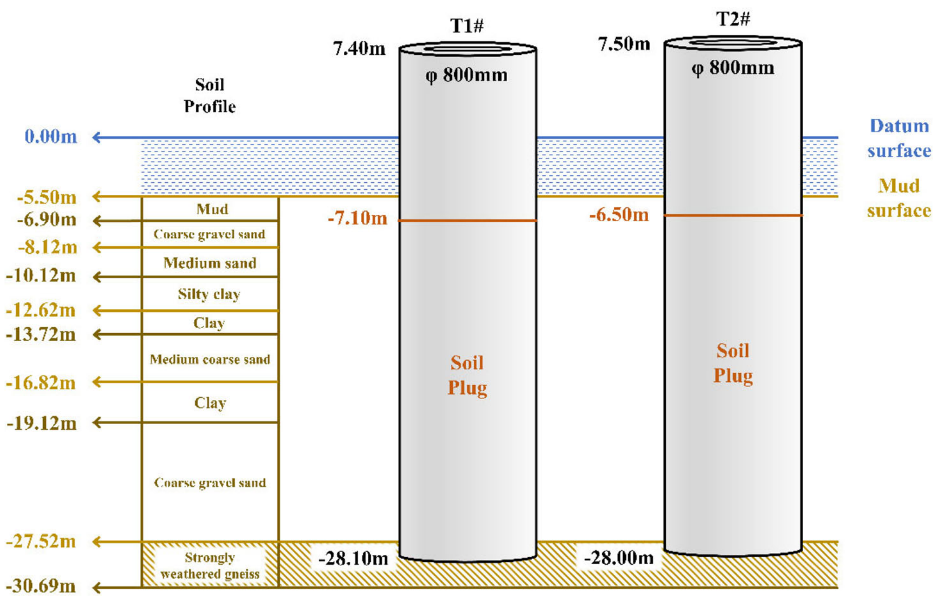

Figure 7. Strata profile and embedment depths of test piles.

4.1.1. During pile driving

There are two main purposes for dynamic monitoring of the pile driving process. One is to judge the performance of the whole impact system according to the impact force and transferred energy. The other is to inspect the pile integrity and to control the damage caused by ultimate tensile and compressive stresses.

The dynamic signals monitored in the pile driving process were converted into the following indices and corresponded to the pile-soil system response to hammer excitation.

The maximum displacement is obtained by the quadratic integration of acceleration with time, and the maximum impact force is directly measured by the strain transducers. According to the wave dynamics, the maximum energy actually transferred by hammer to the pile can be calculated as:

$$E_{max} = \int_0^T Fvdt \tag{5}$$

where T is the end time of sampling; F is the measured impact force; v is the measured velocity.

The tensile stress at the measuring section can be calculated according to Equation (6). Generally, the maximum tensile stress was measured when the pile tip passed through the hard stratum to enter the soft one.

$$\sigma_t = \frac{1}{2A}\left[Zv\left(t_1 + \frac{2l}{c}\right) - F\left(t_1 + \frac{2l}{c}\right) - Zv\left(t_1 + \frac{2l-2x}{c}\right) - F\left(t_1 + \frac{2l-2x}{c}\right)\right] \tag{6}$$

where σ_t is the maximum tensile stress, kPa; A is the section area, m^2; Z is the impedance of pile shaft $= EA/c$, kN·s/m; E is the elastic modulus of the pile material, MPa; c is the velocity of stress wave, m/s; t_1 is the time corresponding to the first peak of velocity wave, ms; l is the length of pile below the measuring section, m; x is the distance between the calculation point and the measuring section, m.

The maximum compressive stress is generally observed when the pile tip enters the hard stratum based on:

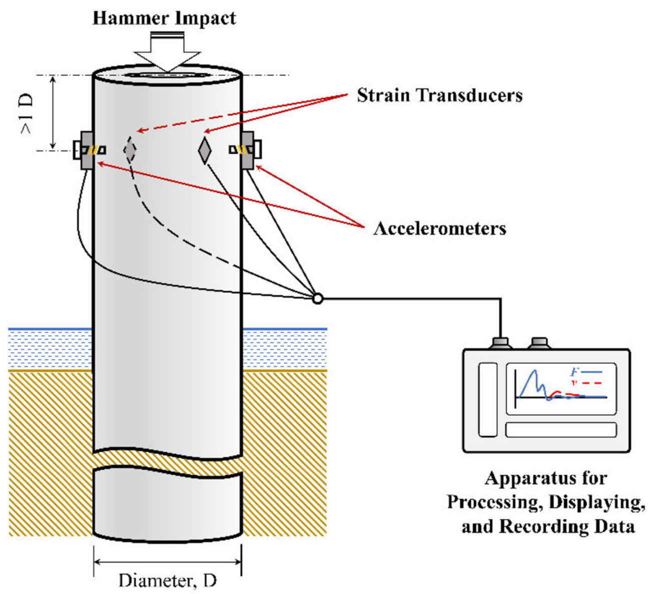

Figure 8. Schematic diagram of measuring system of Pile Dynamic Analyzer.

$$\sigma_{cmax} = F_{cmax}/A \tag{7}$$

where F_{cmax} is the maximum impact force.

4.1.2. After pile installation

After pile installation, the high strain dynamic tests were employed twice, with an interval of 14 days, to determine the axial ultimate compressive bearing capacity and the strength recovery of soil near the perimeter of the test pile.

Generally, in the high strain dynamic test, the bearing capacity of driven steel pipe pile can be determined by driving formula or wave equation solution.

Among various empirical dynamic driving formulas, the most famous and widely used one is Hiley Formula based on the law of energy conservation and momentum transfer. The bearing capacity is estimated mainly according to the final penetration or blow counts as:

$$R_s = \frac{\eta \xi W_h H}{S + C/2} \tag{8}$$

where η is the impact efficiency; ξ is the energy reduction factor; W_h is the hammer weight; H is the drop distance; S is the final penetration; and C is the total elastic deformation of the pile-soil system.

There are two kinds of methods based on wave equation solution: Case Method and Case Pile Wave Analysis Program (CAPWAP) numerical solution (Rausche, Goble, and Likins 1985). These method assumed that the pile is a linear elastic bar. Under external force, the stress wave propagates along it and each section of the bar moves axially and produces corresponding displacement, which satisfies the D̀Alembert solution of the one-dimensional wave equation:

$$u(x,t) = f(x - ct) + g(x + ct) \tag{9}$$

where u is the displacement at a position x along the bar at time t and c is the wave speed at the same time and location.

Case Method adds three specific assumptions for the pile-soil interface models: (1) for the pile, assuming constant index properties along the whole pile, including the impedance; (2) for the soil dynamic resistance around the pile, assuming the resistance concentrating at the pile tip is proportional to the particle velocity and the impedance at the pile tip as Equation (10); (3) for the soil static resistance, assuming ideal rigid-plastic displacement of the pile.

The bearing capacity is calculated as (Rausche et al. 2004):

$$R_d(t) = J_c \cdot Z \cdot v_p(t) \tag{10}$$

$$R_s = \frac{1}{2}\left[(1 - J_c)(F + Zv)_t + (1 + j_c)(F - Zv)_{t+(2l/c)}\right] \tag{11}$$

where J_c is the Case damping factor; t and $t + (2l/c)$ are the time corresponding to the first and second peaks of velocity wave.

CAPWAP, as a famous program, provides a numerical solution of Equation (9) which is based on the lumped spring mass (Smith) model (Smith 1960). It further modifies the model assumptions of Case Method: (1) for the pile model, it is divided into several units which show different index properties for every single one; (2) for the soil dynamic resistance, it assumes to exist concurrently at the pile tip and sides, and change with the static resistance and particle velocity as proposed in Equation (12); (3) for the soil static resistance, assuming ideal elastoplastic displacement of the pile-soil. These assumptions are closer to the actual situation than Case Methods̀. In addition, the damping and micro-cracks are also considered.

$$R_d(t) = J_s \cdot R_s(t) \cdot v_p(t) \tag{12}$$

The ultimate compressive bearing capacity, R_s, is determined by the iterative fitting method of measured curves (Sakr 2013): assuming the pile model parameters (e.g., number of units, sectional area, wave velocity, modulus) and soil model parameters (e.g., resistance, shaft and toe quakes, damping). The measured velocity signal is taken as the input of pile top boundary condition, and the wave equation is solved by using the characteristic method to get the force - time curve. If the calculated force curve is not consistent with the measured one, the parameters of pile and soil models would be adjusted and the iterative calculations are carried out again until the curves reaching the maximum agreement. In other words, the match quality (MQ) defined as the sum of the absolute values of the differences between calculated and measured quantity meets the pre-determined standard.

4.2. Principle and arrangement of static load test

Static load tests are generally divided into axial compression and uplift load tests, to determine the ultimate compressive and uplift bearing capacities of test piles, respectively. In this study, two full-scale open-ended steel pipe piles with same dimensions were used as test piles, six anchor piles were used as reaction piles, and two PHC piles were used as reference piles as shown in Figure 6.

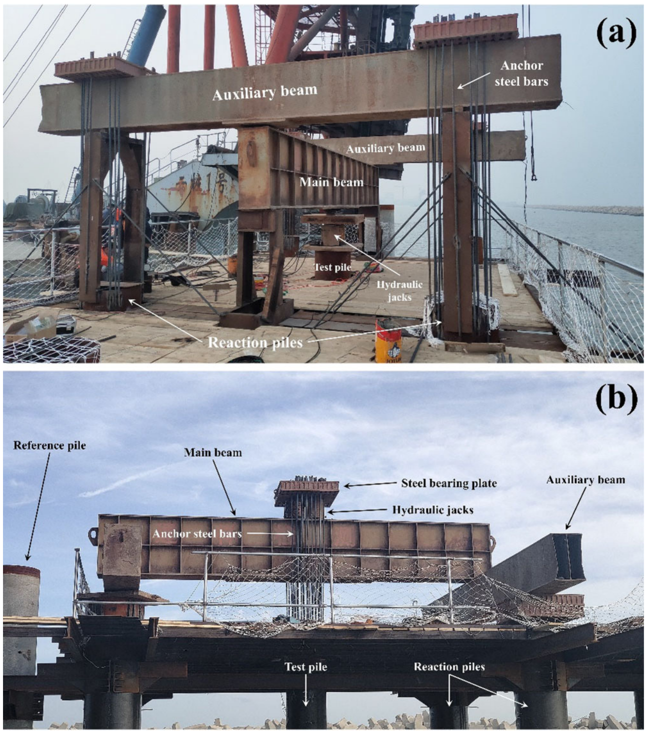

Figure 9. Visual graphs of axial compression load test setup (a) and axial uplift load test setup (b).

4.2.1. Compression load test

The static compression load tests were performed in accordance with ASTM D1143/D1143M-20. The axial load of the test pile was provided by hydraulic jacks, which were situated between the pile top and the main beam. The anchor piles acting as reaction piles were connected with the steel bearing plate by welded anchor steel bars. The applied load was controlled by JCQ-503B semi-automatic static load testing system. Four UPM-50 capacitive grating sensors were set symmetrically around the pile top and kept in the same horizontal plane, recording the axial displacement of the test pile. The oblique view of loading test apparatus is shown in Figure 9.

The axial compression static load test adopted the quick maintain load method and hierarchical loading method. In the loading stage, single step of load was maintained for 60 min, and the load increment was 1/10 of the designed maximum load. The first step was directly loaded at twice the load increment. The displacement of the pile top was recorded at 5, 15, 30 and 60 min during the load maintenance. In the unloading stage, the load was removed in decrements of 1/5 of designed maximum load. The load was maintained for 30 min and the displacement was recorded at 5, 15, and 30 min. When all loads were removed, it was still maintained for 2 hours. The recording time was 5, 15, 30, 60, 90, and 120 min. During the test, the change in strain distribution along the pile body under each loading step was detected by BOTDR sensing optical cable and FBG sensors.

According to the measured data, the pile top deformation, axial strain and stress, lateral friction and tip resistance of test pile can be calculated. The design loading and unloading load steps are shown in Table 4.

Table 4. Loading and unloading steps of axial compression test (unit: kN).

Pile	Steps	1	2	3	4	5	6	7	8	9
T1 (kN)	Loading	1440	2160	2880	3600	4320	5040	5760	6480	7200
	Unloading	5760	4320	2880	1440	0				
T2 (kN)	Loading	1600	2400	3200	4000	4800	5600	6400	7200	8000
	Unloading	6400	4800	3200	1600	0				

Table 5. Loading and unloading steps of axial uplift test (unit: kN).

T1 steps	1	2	3	4	5	6	7	8	9
Loading (kN)	600	900	1200	1500	1800	2100	2400	2700	3000
Unloading (kN)	2400	1800	1200	600	0				

4.2.2. Uplift load test

Axial uplift static load test was carried out after 3 days of the compression load test in accordance with ASTM D3689/D3689M-07. The main beam and auxiliary beams were placed on anchor piles, to provide the anchor force and the hydraulic jacks were placed on the main beam. A heavy steel bearing plate connected with the test pile through welded anchor steel bars was placed upon the hydraulic jacks. The uplift load test adopted slow maintain load method and hierarchical loading method. After each step of load increment, the axial uplift displacement of pile top was measured at 5, 15, 30, 45 and 60 min. The measurement continued until the displacement was lower than 0.1 mm per hour. After the final load increment, all loads were removed in decrements of 1/5 of the designed maximum load with 1 h between decrements. The displacement measurement was recorded at 5, 15, 30, 45, and 60 min at each step. The residual displacement was recorded for 3 hours after the final decrement. The design loading and unloading load levels are shown in Table 5.

5. Results and discussions

5.1. Pile driving analysis

5.1.1. High strain dynamic test

The high strain dynamic test data were recorded by strain transducers and accelerometers, then processed by automatic signal matching program with Foundation Engineering Institute Pile Wave Analysis Program by Characteristics (FEIPWAPC). Table 6 summarizes the computed key mechanical parameters during pile driving.

Blow count and pile drivability analysis play an important role in pile driving. Piles T1 and T2 were driven into marine soil using D138 diesel hammer of 13.8 ton with the depths of 22.6 m and 22.5 m, respectively. It is found that the blow counts of pile T1 was 62 more than that of pile T2, corresponding to larger embedment depth of 0.1 m. According to the blow counts per unit penetration (500 mm) versus pile driving depth in Figure 10, when the pile tip was driven near the bearing stratum, the number of hammer blows increased rapidly and the penetration decreased sharply from dozens to a few millimeters. This proves that the bearing stratum had good engineering properties and met the requirements of foundation bearing capacity.

Figure 11 depicts the variation of maximum transferred energy and compressive stress of piles T1 and T2. The graph

Table 6. Pile driving analysis results summary.

Pile	Blow count	Maximum transferred energy (kJ)	Maximum impact force (kN)	Maximum compressive stress (MPa)	Maximum tensile stress (MPa)	Maximum displacement (mm)
T1	829	54.4–260.0	3411–10708	68.8–211.6	9.5–103.2	23.7–70.0
T2	767	52.3–120.5	3467–7193	75.7–159.7	3.4–87.5	23.7–71.6

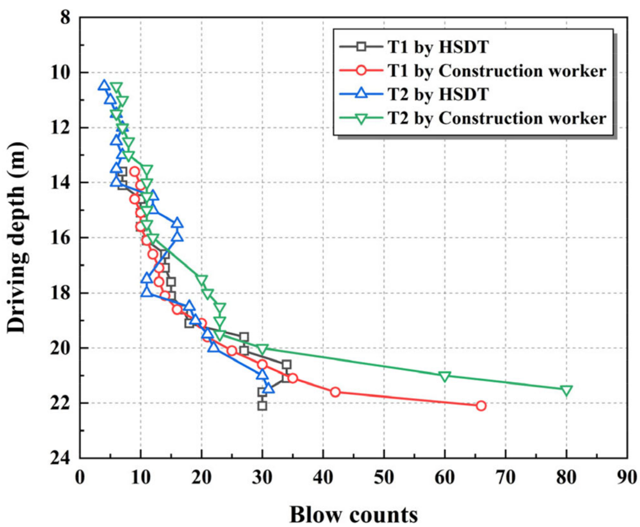

Figure 10. Blows counted by high strain dynamic test and construction worker.

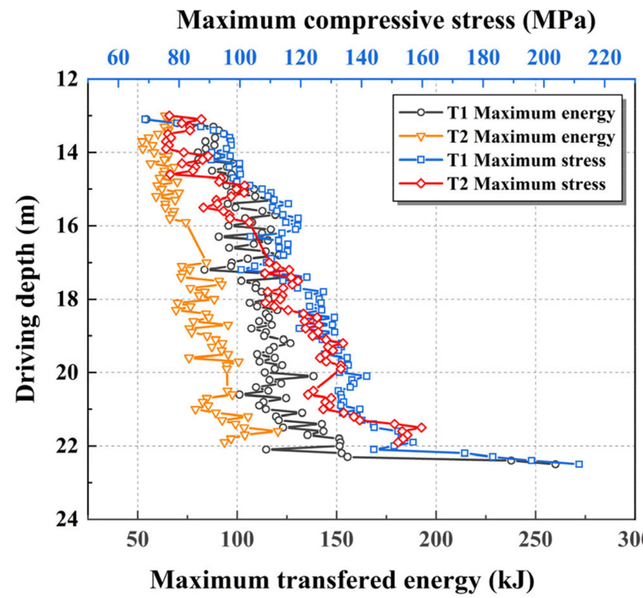

Figure 11. Variation of maximum transferred energy and compressive stress.

also shows that the upper limits of maximum transferred energy, impact force, and stress for pile T1 were higher than that of pile T2 owing to larger embedment depth. For each test pile, these key mechanical parameters in Table 6 increased with the driving depth of the pile, except for the maximum downward displacement. In addition, the variation trend of the maximum compressive stress had a good correlation with that of the maximum transferred energy. This indicates that the main measurement error (i.e., nonlinearity of pile material) in high strain dynamic test can be avoided here since the steel pipe piles of offshore platform foundations were generally homogeneous and high-strength.

According to ASTM A252-19, the yield strength of test steel pipe piles was 310 MPa, and the tensile strength was 455 MPa. The maximum dynamic compressive and tensile stressed did not exceed 90% of yield stress of the pile body, implying that the pile structure was intact during testing.

Energy transferred to the pile during the whole process was used to determine the match degree and efficient operation gear of impact device, including the diesel hammer. The ratio of the actually transferred energy to the manufacturer output energy is called the impact efficiency. For steel piles impacted by diesel hammer, the value is generally 26% $\sim$ 50%. In this study, the output energy of 13.8-ton hammer in second gear is 344.85 kJ. Hence, the efficiency of chosen impact device was 22.60% $\sim$ 32.85%. However, the accumulation of high level of excitation energy might result in the shaking of the pile to make the sensors fall off from the pile body, leading to the data loss of pile T1 at the last 0.1 m and pile T2 at the last 0.6 m. Considering this accident, it could be proven that the hammer output energy can effectively transmit to the pile during the process of pile driving. Therefore, the working efficiency of pile hammer system could meet the design requirements.

5.1.2. Fiber optic sensing

Based on the driving depth and the monitoring data obtained by FBG demodulator, nine fiber Bragg grating strain sensors on one side of each test pile were divided into three groups for analysis. According to the installation position, they were named as "FBG 1 $\sim$ FBG 9" in a distance sequence, in which "FBG 1" was closest to the pile tip as shown in Figure 4. Results of FBG 1 to FBG 4 are plotted in Figure 12, corresponding to the strain variation at 1.2, 4.2, 7.2 and 10.2 m away from the pile tip. Other results of remaining sensors FBG 5 to FBG 9 are plotted in Figures 13 and 14. The reported data in these figures were already incorporated the effect of temperature calibration on FBG sensors.

Figure 12 shows that the whole driving process lasted about 1050 seconds, after which the strain only fluctuated slightly. It seems that the set of curves for FBG 1 and FBG 2, and for FBG 3 and FBG 4 were similar. During pile driving, the stress state of the pile was controlled by the impact force, as well as soil resistance condition. The pile body driven into the soil was subjected to compression, while the part above the mud surface was in tension state. FBG 1, 2 and FBG 3, 4 were in tension at the beginning and then successively turned into compression at about 100 s and 250 s. This difference was due to the increasing distance of sensor to the mud surface.

For the sensors with larger distance (FBG 5, 6) to mud surface as shown in Figure 13, the time from tension to compression state dramatically increased to more than 800 s, in comparison with the results in Figure 12. For case of

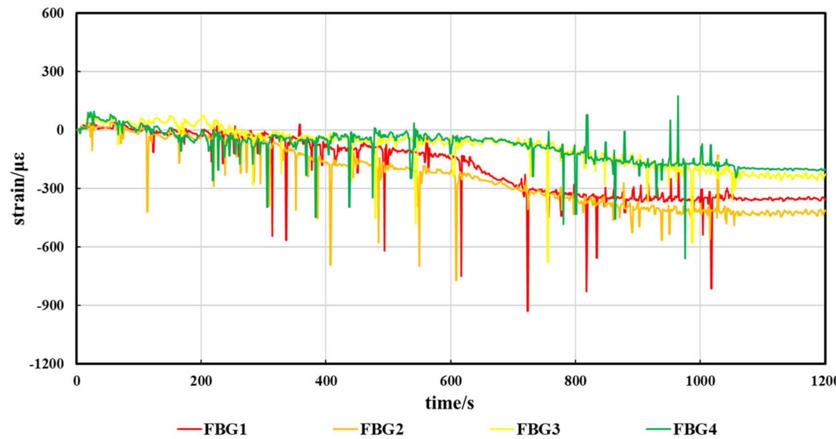

Figure 12. FBG strain diagram of T1 “Side A” at 1.2 m∼10.2m.

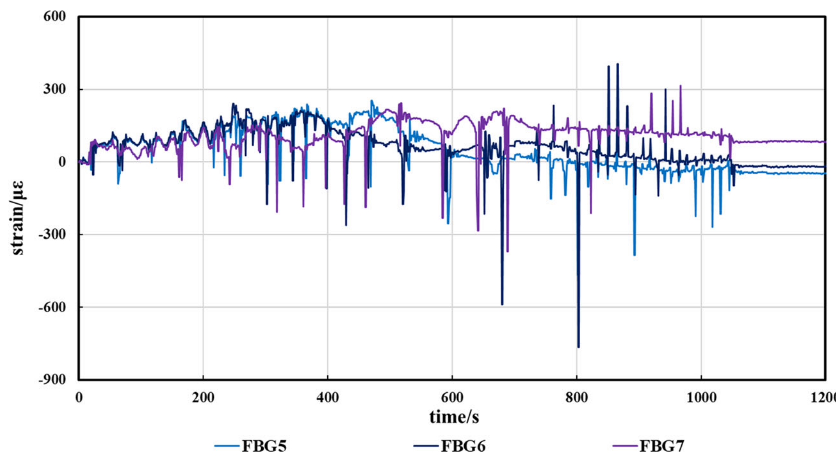

Figure 13. FBG strain diagram of T1 “Side A” at 13.2 m∼19.2m.

FBG 7, it seems that the strain state was in tension during the whole driving process, and the maximum tensile strain was 200 $\mu\varepsilon$. Figures 12 and 13 illustrate that the compressive strain increased with the pile driving process or the length of pile inside the soil.

Figure 14 shows that the curves of sensors FBG 8 and 9 were different from that at lower positions as shown in Figures 12 and 13. This was mainly because the sensors FBG 8 and 9 were not driven into soil during the whole process and not subjected to side friction. Sensors FBG 8 and 9 were in tension at first and then changed into compression state. The change time was earlier for FBG 8 at a closer position to the pile tip. These two sensors measured huge tensile strain in 300 s ∼ 800 s, then the tensile strain changed into compressive strain which increased gradually until the end of driving process. When major part of pile was penetrated into the soil, this lead to a significant anchor effect at the end of pile. Hence, the displacement of pile under the same hammer reduced significantly with the increase in the distance of pile inside the soil. Therefore, at the end of pile driving (i.e., 800 s–1050s), the pile top was subjected to significant compression under hammer with the fixed pile end inside soil. This corresponded to the sharp increase in compressive strain of FBG 9.

Similar results were also observed for pile T2 “Side A” in Figure 15.

The maximum compressive stress and tensile stress of test piles monitored by different methods are summarized in Table 7.

The comparisons of high strain testing and fiber optic techniques on monitoring the pile driving process are presented as follows:

1. As the steel pipe piles used in offshore platform foundations were generally long, the impact force generated by the hammer often led to the bending deformation and eccentric load of the upper part of the pile above soil. Consequently, the relatively large tensile strain was observed in the pile body. This large tensile strain may be a considerable problem in offshore pile foundation construction.
2. The maximum tensile stress calculated from all three methods did not exceed the tensile strength (e.g., 455MPa) of the pile material. Due to the deeper embedment of T2, its maximum compressive and tensile stresses in the final stage were larger than that of T1. This phenomenon was captured by both FBG and BOTDR techniques. However, the results of high strain tests showed an opposite trend. This was mainly due to the earlier data loss of T2 with the sensors falling from the pile.

Hence, it can be conducted that the fiber optic sensing technique was suitable for the offshore foundation, which may provide more reliable data in complex geological conditions.

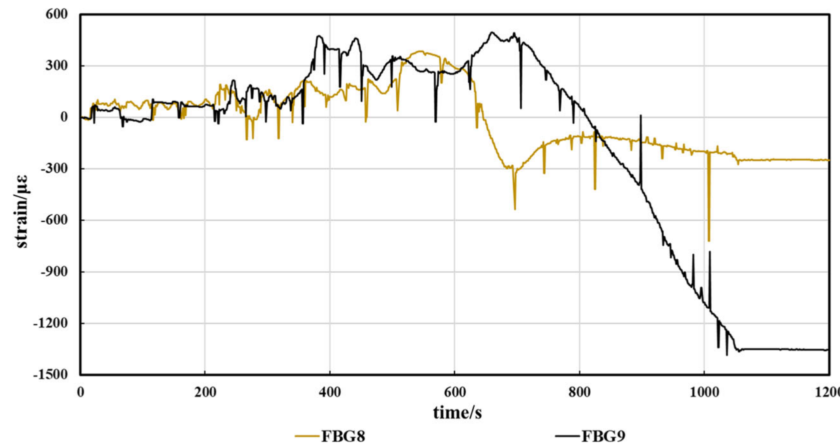

Figure 14. FBG strain diagram of T1 "Side A" at 24.2 m∼29.2m.

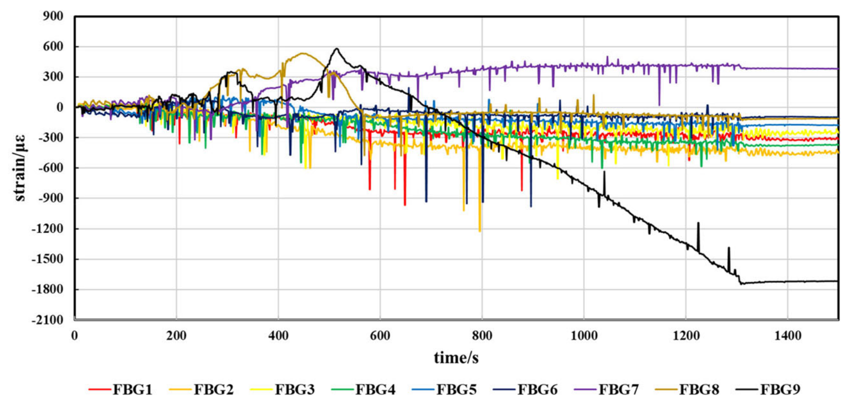

Figure 15. FBG strain diagram of T2 "Side A".

Table 7. Comparison of maximum stresses by high strain dynamic test and fiber optic sensing.

Pile	Test results (MPa)	High strain test	FBG	BOTDR
T1	Tensile stress	103.21	115.90	56.26
	Compressive stress	211.61	284.18	99.54
T2	Tensile stress	87.53	119.25	72.00
	Compressive stress	159.73	358.09	131.64

5.2. Vertical bearing capacity

5.2.1. Dynamic load test results

In this paper, FEIPWAPC developed by CABR, which is improved from CAPWAP considering the softening and hardening of soil, was used to process high strain dynamic test data.

The pile bearing capacity evaluated through pile driving formulas were based on the blow counts as listed in Table 8. It is clear that the calculated values were not consistent with the measured ones. Moreover, the blows counted by the Pile Dynamic Analyzer and the construction worker were different during the driving process, especially at the final stage as shown in Figure 10. It should be noted that the measured blow counts were recorded when the pile tip elevation reaches −13.0 m, because the pile needs to be driven into a certain depth of mud in advance to ensure the vertical stability of the piles in the actual driving process. Although the blow counts calculated by the FEIPWAPC program in restrike tests were higher than that of the initial strike test, the calculated values and measured values cannot match well. Still, many factors, such as cushion characteristics, pile length, and elastic-plastic characteristics of pile perimeter soils affect the accuracy of the pile driving formula. Hence, a pile driving formula based on the final penetration per blow is only applicable to a certain type or length of pile and not reliable to calculate bearing capacity in this study.

Case Method can roughly provide the estimated value of ultimate bearing capacity in the field. However, its accuracy mainly depends on the determination of the only unknown quantity J_c, which is a dimensionless empirical factor. In the actual calculation, it is necessary to consider the local experience of soil properties and the results of the CAPWAP fitting method. This means the reasonable value of J_c is always a difficult problem for testers. Moreover, because the pile-soil models are too simplified, the accuracy and objectivity of analysis results cannot meet the requirements. Considering that there is no previous experience for reference, Case Method is not adopted.

Tables 9 and 10 show the computed results by FEIPWAPC. The computed results of pile shaft, toe and total resistance were larger in restrike test than that in initial strike test for both test piles. This implies that the soil strength around the pile had been effectively restored when excessive pore pressure was dissipated after pile driving. The enhancement of toe resistance was higher than that of shaft resistance, while the total soil resistance was mainly provided by side friction.

Figure 16 shows the force versus time curves for T1 and T2 in both initial strike and restrike tests. The computed

Table 8. Calculated and measured values of blow counts.

Pile	Calculated value in initial strike test	Calculated value in restrike test	Measured value
T1	123	672	829
T2	299	1000	767

Table 9. FEIPWAPC analysis parameters and results for pile T1.

Test		Quake (mm)	Smith damping factor (s/m)	Resistance (kN)	MQ
Initial strike	Shaft	6.15	12.01	4102.0	3.84
	Toe	2.50	0.96	2033.0	
	Total	–	–	6135.0	
Restrike	Shaft	4.93	10.18	5472.0	3.45
	Toe	1.50	1.05	3033.0	
	Total	–	–	8505.0	

force (F) curves were fitted based on the measured velocity-impedance (Zv) curves. It can be observed that there was a good correlation between the measured force curves and computed ones at both initial strike and restrike tests. The match qualities for piles T1 and T2 satisfy the pre-determined standard. It shows that the pile-soil model parameters in the fitting calculation are basically reasonable and the estimated bearing capacity is reliable.

5.2.2. Static load test results

During the static load test, FBG and BOTDR sensing techniques were used to obtain the penetration characteristics of driven pile including strain, axial force and side friction, other than the conventional method.

In general, the load-displacement curve can be divided into three regimes (Sakr 2013): two linear stages, which was connected by a nonlinear stage. The first linear stage represents the elastic deformation state of the pile body and the soil at the pile tip. The nonlinear stage corresponds to the critical state of maximum skin friction for the soil at the pile side. Finally, the second linear stage represents that the pile body is broken or the soil at the pile tip is damaged, i.e., the displacement of pile top increases rapidly and continuously under constant load.

Figure 17 shows the loading and unloading increments for piles T1 and T2. In the loading stage, except for the large instantaneous settlement of the first load increment, the displacement of the other load increments increased gradually. In the unloading stage, the rebound displacement of each unloading decrement increased gradually. It should be pointed out that there was no obvious second linear segment (i.e., plunging failure) in load-displacement curves.

The reasons for the curve shape without obvious steep drop in the static load compression test are as follows: (1) the load tests were applied on the offshore temporary platform, so the test piles were not loaded to failure for the safety of test personnel; and (2) compared with the designed value, the test load had already met the design requirements.

The test results in Table 11 suggest that the soil at the pile tip was not damaged, and the soil at the pile side did not reached the maximum friction state. Hence, the test piles could continue to use as an engineering pile in the normal project, resisting loads at higher displacement levels without plunging failure or pile fracture.

For the case with clear failure stage, the ultimate bearing capacity can be easily obtained at the starting point of the obvious segment. However for the case without secondary linear segment, the bearing capacity needs to be estimated based on the total settlement of pile top. The total settlement of pile top consisted of axial compression deformation

Table 10. FEIPWAPC analysis parameters and results for pile T2.

Test		Quake (mm)	Smith damping factor (s/m)	Resistance (kN)	MQ
Initial strike	Shaft	6.97	27.73	3822.0	3.85
	Toe	9.50	0.12	2133.0	
	Total	–	–	5925.0	
Restrike	Shaft	7.40	18.57	5082.0	3.97
	Toe	6.50	0.25	3120.0	
	Total	–	–	8202.0	

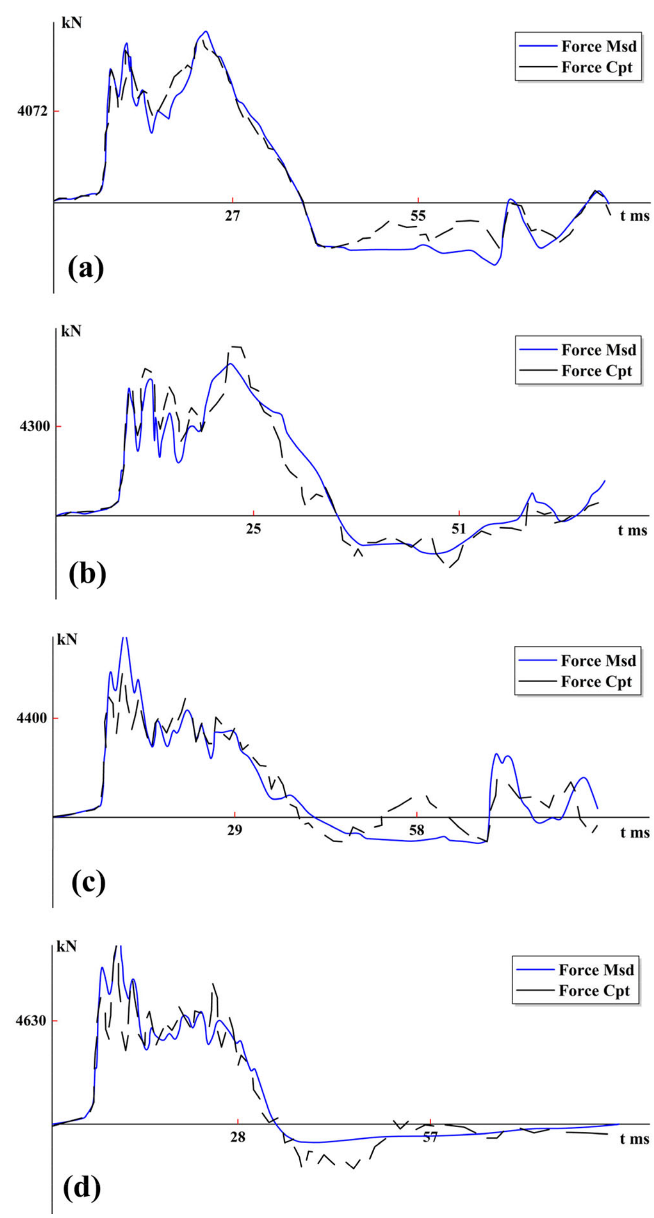

Figure 16. FEIPWAPC fitting results of force curves: (a) T1 in initial strike test, (b) T1 in restrike test, (c) T2 in initial strike test, and (d) T2 in restrike test.

of pile shaft and soil displacement at pile tip. The deformation of pile shaft was a function of loads, soil properties and pile characteristics. While the soil displacement at pile tip was mainly controlled by the embedment depth and diameter of pile. Hence, the total settlement at load of ultimate bearing capacity consisted of three parts: compression deformation of pile body, the function of pile diameter, and the correction term. Thus, the axial ultimate bearing capacity of pile can be deduced by:

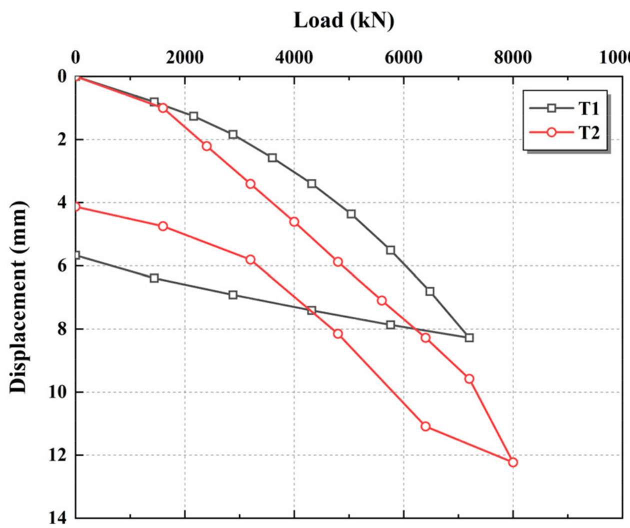

Figure 17. Axial static compression load test results of pile T1 and T2.

$$S = \frac{2WL}{AE_p} + F(D) + b \tag{13}$$

where W is the design value of pile bearing capacity, L is the pile length, A is the sectional area, E_p is Young's modulus of the pile material, D is the pile diameter and b is the correction term.

The axial ultimate bearing capacity of the pile can be determined by using Davisson (Davisson 1972) and Federal Highway Administration (FHWA) failure criteria (Paikowsky and Whitman 1990) according to the settlement criterion. In the FHWA (5%) failure criterion, the bearing capacity was defined as the load corresponding to the displacement of 5% of the pile diameter. In Davisson's criterion, it was defined as the load corresponding to the total settlement S illustrated in Equation (14), which is the most widely used quantitative formula based on the rudiment of:

$$S = \frac{PL}{AE_p} + \frac{D}{120} + 4(mm) \tag{14}$$

where P is the ultimate load on the pile top.

The test piles in this study have not been loaded to plunging failure, and the pile top deformation could not meet the requirements of FHWA (5%) failure criterion (i.e., 40 mm). Hence, the static compressive capacities of T1 and T2 were determined using both high strain tests and Davisson's criterion, as presented in Table 12. Comparing the results of both static and dynamic load tests, it is found that the estimation of axial ultimate bearing capacities of

Table 11. Loads, settlement and rebound displacement of test piles.

Static load test	Pile	Maximum loads (kN)	Maximum displacement (mm)	Maximum rebound displacement (mm)	Rebound rate (%)
Compression	T1	7200	8.28	2.61	31.52
	T2	8000	12.23	8.10	66.23
Uplift	T1	3000	8.69	4.79	55.12

Table 12. Summary of bearing capacity by dynamic and static loading tests.

Pile	Initial strike test (kN)	Restrike test (kN)	Static load test (kN) (Davisson's criterion)
T1	6135	8505	7459
T2	5925	8202	7473

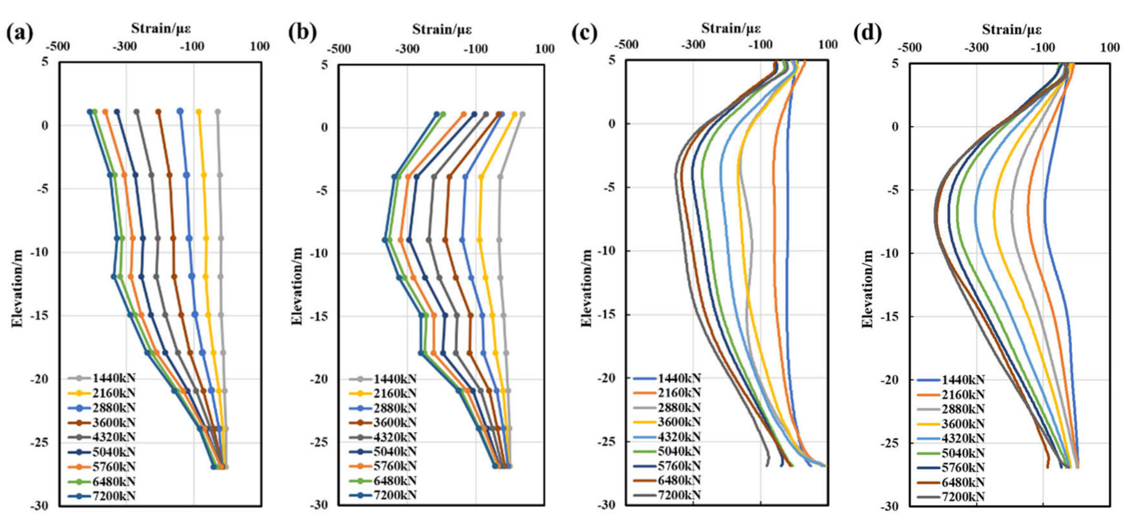

Figure 18. The distribution curves of axial strain along the elevation gradient: (a) "Side A" of T1 FBG, (b) "Side B" of T1 FBG, (c) "Side A" of T1 BOTDR, (d) "Side B" of T1 BOTDR.

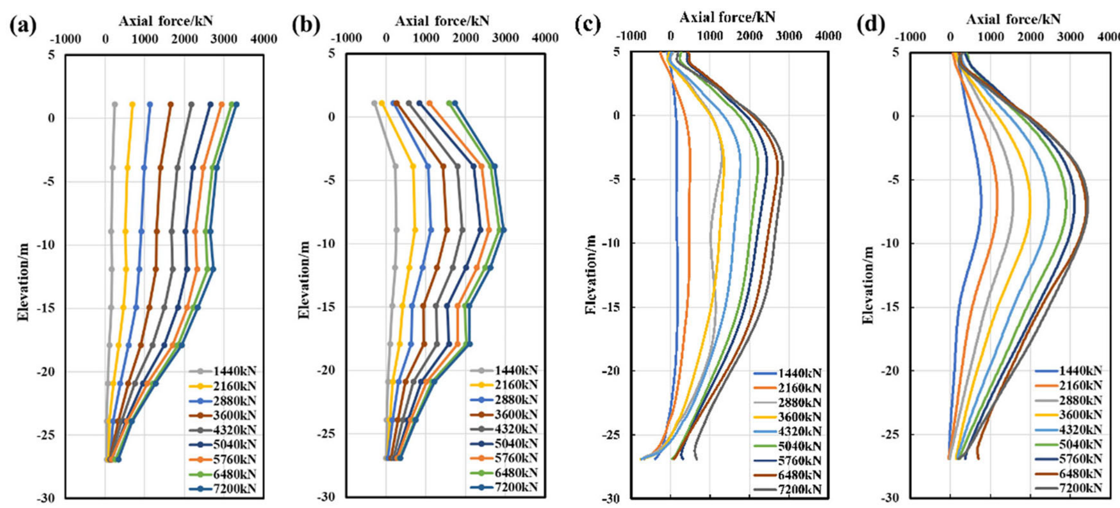

Figure 19. The distribution curves of axial force along the elevation gradient: (a) “Side A” of T1 FBG, (b) “Side B” of T1 FBG, (c) “Side A” of T1 BOTDR, (d) “Side B” of T1 BOTDR.

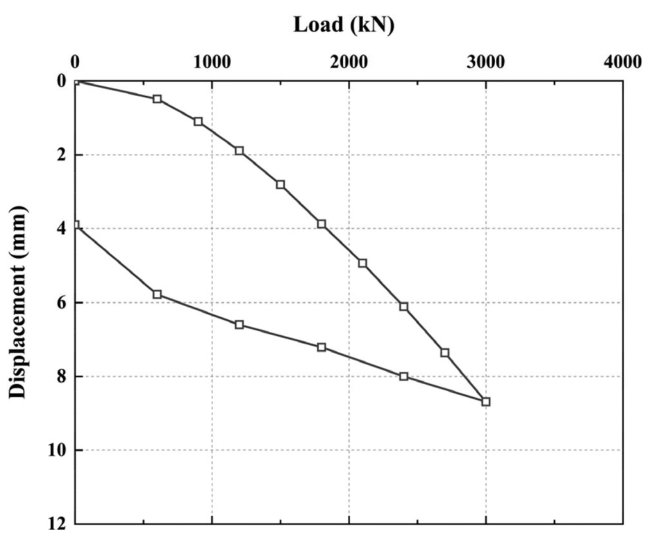

Figure 20. Axial static uplift load test result of T1.

both test piles by Davisson's criterion was relatively smaller than that of restrike tests, but larger than that of initial strike tests. It's obvious that the actual bearing capacity of pile T2 must be higher than the estimation results of Davisson's criterion, because there has not been plunging failure under the load of 8000 kN. This suggests that the error of determination of ultimate bearing capacity using different methods was relatively high, indicating a high degree of uncertainty on this parameter. More importantly, the ultimate bearing capacity was one of the most important indices in the safety of the pile foundation. Hence, it is often necessary to combine a variety of means, obtaining a more accurate and reasonable calculation of the ultimate bearing capacity of test piles.

5.3. Load-transferring characteristics

Figures 18 and 19 depict the axial strain and force evolution of T1 obtained by both FBG and BOTDR during the static compression load test. It can be found that the magnitude of strain and force and its variation along pile shaft were very close using FBG or BOTDR, except for the upper part of “Side A” strain curve. The difference of FBG “Side A” curves might come from the large error of monitoring results of FBG 7 $\sim$ FBG 9 sensors. Nevertheless, the consistency of test results between FBG and BOTDR confirmed the accuracy of fiber optic detection. BOTDR provides more detailed data about load transfer relations due to its Distributed-Testing characteristics.

With the increase of the applied loads on the pile top, the compressive strain at the same position along the pile shaft elevation increased gradually. At each load stage, the maximum compressive strain appeared at the elevation of -5.50 m, corresponding to the elevation of the mud surface. Above the soil surface, the strain of pile gradually increased to the pile top. Meanwhile, for the section under the soil surface, the strain of pile gradually decreased to the pile tip.

It can also be observed that the strain and force at the pile end was merely small. This indicated that the large-diameter long steel pipe pile used in this study belonged to friction pile, and the pile tip resistance has not been fully exerted. Thus, it can be deduced that the ultimate bearing capacity of the piles was larger than the test results reported. In this study, eighty percent of the compression of the pile shaft mainly occurred in the upper 20 m of the pile, and the settlement of the pile top of the long steel pipe pile was mainly caused by the compression of the pile shaft, rather than the soil displacement at the pile tip.

5.4. Uplift bearing capacity

Figure 20 presents the relationship between displacement and load during uplift test of T1. In the loading stage, the displacement increased gradually as the load increased. In the unloading stage, the rebound displacement increased gradually. The test results are shown in Table 11. Still, there was no obvious second linear segment in the load-displacement curve. The maximum load was taken as the ultimate uplift bearing capacity (i.e., 3000 kN).

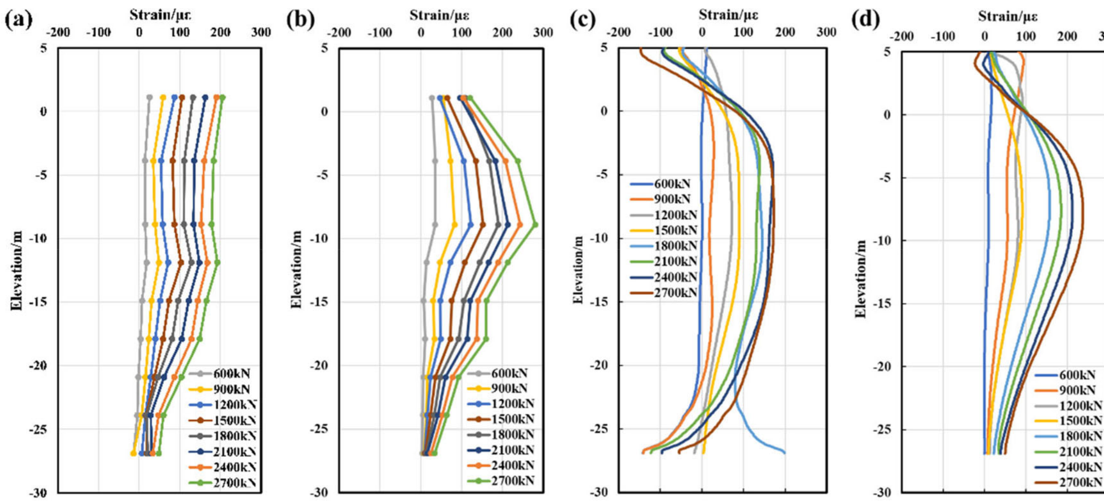

Figure 21. The distribution curves of axial strain along the elevation gradient: (a) "Side A" of T1 FBG, (b) "Side B" of T1 FBG, (c) "Side A" of T1 BOTDR, (d) "Side B" of T1 BOTDR.

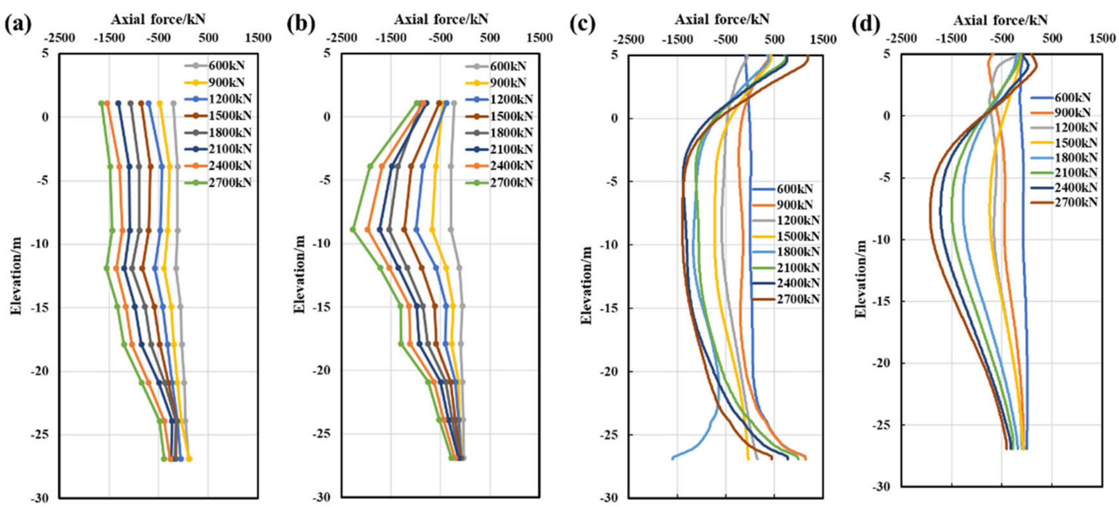

Figure 22. The distribution curves of axial force along the elevation gradient: (a) "Side A" of T1 FBG, (b) "Side B" of T1 FBG, (c) "Side A" of T1 BOTDR, (d) "Side B" of T1 BOTDR.

Figures 21 and 22 show the strain and axial force evolution of T1 obtained by both FBG and BOTDR during the static uplift load test.

Similar to that of compression test, the results of strain and axial force evolution recorded by FBG was consistent with that of BOTDR. The maximum tensile strain appeared at the soil surface of -5.50 m. and the minimum tensile strain was at the pile tip. The tensile stress of pile was mainly concentrated in the upper part. Under the same load stage, the strain measured by FBG was greater than that measured by BOTDR, and the accuracy maybe worse than that measured by BOTDR. Note that, the test result above water level was certainly scattered, which was mainly due to the tail fiber of the optical cable being easily disturbed near the pile top.

6. Conclusions

The pile testing site is located in Ganyu Port District, Jiangsu Province of China. The high strain dynamic tests including initial strike and restrike tests were adopted to monitor the stress condition and transferred energy during pile driving and estimate the bearing capacities and integrity of single test pile. After a period of interruption, the static load tests including axial compression and uplift load tests were performed to estimate ultimate bearing capacities. FBG and BOTDR fiber optic sensing techniques were applied simultaneously in both pile driving process and static load tests in order to explore features of soil-pile interaction and load transfer mechanisms. The following specific conclusions may be drawn:

1. In the process of pile driving, the fiber optic strain data show that there was eccentric load on the upper part of both test piles, and the degree of eccentricity gradually decreased. Through the data analyzed by PDA of high strain tests, it is found that the maximum dynamic stresses were within the yield stress of the pile shaft. Also, it could be proven that the hammer output energy could effectively transmit to the pile and the working

efficiency of pile hammer and pile dimensions' system could meet the design requirements.

2. The results of double high strain dynamic tests and fitting analysis indicate that test piles were complete. After a 14-day elapsed period, the side friction and tip resistance have been improved significantly. It can be seen from the measured and calculated force-time curves that the main soil resistance of the pile was concentrated in the lower part of the pile body, and the force curve appears convex at 2L/c, which indicates that the strongly weathered gneiss is sufficient as the bearing stratum. However, the application of high strain dynamic test to determine the bearing capacity of pile depends on the engineering judgment and experience of testers hugely, and suffers from multi-solution problems. In areas where there is a lack of adequate previous experience in pile driving, the application is even more limited.
3. Through the static uplift load test, the maximum load value was taken as the ultimate uplift bearing capacity. The ultimate compression bearing capacities could be determined by the load-displacement curve. Since the test piles were not loaded to plunging failure, the compression bearing capacity obtained by Davisson's criterion was smaller than that obtained in the high strain tests. To explore an ideal method analyzing the load-displacement curve without obvious second linear segment is still a significant problem to be solved.
4. Based on the analysis of the monitoring results during static load tests by fiber optic sensing systems, it is found that the strain, axial force and side friction distribution have strong regularities. In the axial compression load test, with the increase of loading, the compressive strain and axial force of the pile body gradually increased, and the pile body was subject to upward positive friction. In the axial uplift load test, with the increase of uplift loading, the tensile strain increased gradually with negative side friction. The settlement in the static load test was mainly caused by the compression of the pile body, and the tip resistance has not been fully exerted, which illustrates that the bearing capacity of the test pile could be further improved.
5. The sensors falling-off and data loss are common problems for high strain tests, especially in complex marine strata. Meanwhile, the load transfer characteristics of steel pipe piles could be determined only by the attached sensors. A set of fiber optic sensing techniques provide an effective method to such problems, with high sensor survival rate and data acquisition reliability.

Disclosure statement

No potential conflict of interest was reported by the authors.

Funding

This work was supported by the National Natural Science Foundation of China under Grant (No. 42072293).

ORCID

Yong-Feng Deng http://orcid.org/0000-0002-8223-8711
Hong-Hu Zhu http://orcid.org/0000-0002-1312-0410

References

ASTM-A252/A252M. 2019. *Standard Specification for Welded and Seamless Steel Pipe Piles*. West Conshohocken, PA: American Society for Testing and Materials.

ASTM-D1143/D1143M. 2020. *Standard Test Methods for Deep Foundation Elements under Static Axial Compressive Load*. West Conshohocken, PA: American Society for Testing and Materials.

ASTM-D3689/D3689M. 2013. *Standard Test Methods for Deep Foundations under Static Axial Tensile Load*. West Conshohocken, PA: American Society for Testing and Materials.

ASTM-D4945. 2017. *Standard Test Method for High-Strain Dynamic Testing of Deep Foundations*. West Conshohocken, PA: American Society for Testing and Materials.

Barrias, A., J. R. Casas, and S. Villalba. 2016. A Review of Distributed Optical Fiber Sensors for Civil Engineering Applications. *Sensors* 16 (5): 748. doi:10.3390/s16050748.

Bian, X., L. L. Zeng, X. Z. Li, X. S. Shi, S. M. Zhou, and F. Q. Li. 2021. Fabric Changes Induced by Super-Absorbent Polymer on Cement and Lime Stabilized Excavated Clayey Soil. *Journal of Rock Mechanics and Geotechnical Engineering* 13 (5): 1124–1135. doi:10.1016/j.jrmge.2021.03.006.

Campanella, C. E., A. Cuccovillo, C. Campanella, A. Yurt, and V. M. N. Passaro. 2018. Fibre Bragg Grating Based Strain Sensors: Review of Technology and Applications. *Sensors* 18 (9): 3115. doi:10.3390/s18093115.

Davisson, M. T. 1972. High Capacity Piles. In *Proc. Lecture Series on Innovations in Foundation Construction*, 81–112. New York: ASCE.

Doherty, P., D. Igoe, G. Murphy, K. Gavin, J. Preston, C. McAvoy, B. W. Byrne, et al. 2015. Field Validation of Fibre Bragg Grating Sensors for Measuring Strain on Driven Steel Piles. *Géotechnique Letters* 5 (2): 74–79. doi:10.1680/geolett.14.00120.

Fattah, M. Y., B. S. Zbar, and F. S. Mustafa. 2017. Vertical Vibration Capacity of a Single Pile in Dry Sand. *Marine Georesources & Geotechnology* 35 (8): 1111–1120. doi:10.1080/1064119X.2017.1294219.

Han, F., M. Prezzi, R. Salgado, and M. Zaheer. 2017. Axial Resistance of Closed-Ended Steel-Pipe Piles Driven in Multilayered Soil. *Journal of Geotechnical and Geoenvironmental Engineering* 143 (3): 04016102. doi:10.1061/(ASCE)GT.1943-5606.0001589.

Lee, W., W. J. Lee, S. B. Lee, and R. Salgado. 2004. Measurement of Pile Load Transfer Using the Fiber Bragg Grating Sensor System. *Canadian Geotechnical Journal* 41 (6): 1222–1232. doi:10.1139/t04-059.

Li, X., G. Dai, M. Zhu, and W. Gong. 2019. Application of Static Loading Tests to Steel Pipe Piles with Large Diameters in Chinese Offshore Wind Farms. *Ocean Engineering* 186: 106041. doi:10.1016/j.oceaneng.2019.05.023.

Lu, Y., B. Shi, G. Q. Wei, S. E. Chen, and D. Zhang. 2012. Application of a Distributed Optical Fiber Sensing Technique in Monitoring the Stress of Precast Piles. *Smart Materials and Structures* 21 (11): 115011. doi:10.1088/0964-1726/21/11/115011.

Mohamad, H., K. Soga, and B. Amatya. 2014. Thermal Strain Sensing of Concrete Piles Using Brillouin Optical Time Domain Reflectometry. *Geotechnical Testing Journal* 37 (2): 20120176. doi:10.1520/GTJ20120176.

Paikowsky, S. G., and R. V. Whitman. 1990. The Effects of Plugging on Pile Performance and Design. *Canadian Geotechnical Journal* 27 (4): 429–440. doi:10.1139/t90-059.

Rausche, F., G. Goble, and G. Likins. 1985. Dynamic Determination of Pile Capacity. *Journal of Geotechnical Engineering* 111 (3): 367–383. doi:10.1061/(ASCE)0733-9410(1985)111:3(367).

Rausche, F., F. Moses, A. Asce, G. Goble, and M. Asce. 2004. Soil Resistance Predictions from Pile Dynamics. *Geotechnical Special Publication* 98: 418–440. doi:10.1061/40743(142)24.

Sakr, M. 2013. Comparison between High Strain Dynamic and Static Load Tests of Helical Piles in Cohesive Soils. *Soil Dynamics and Earthquake Engineering* 54: 20–30. doi:10.1016/j.soildyn.2013.07.010.

Shi, B., H. Z. Xu, B. Chen, D. Zhang, Y. Ding, H. L. Cui, and J. Q. Gao. 2003. A Feasibility Study on the Application of Fiber-Optic Distributed Sensors for Strain Measurement in the Taiwan Strait Tunnel Project. *Marine Georesources & Geotechnology* 21 (3–4): 333–343. doi:10.1080/713773406.

Smith, E. A. L. 1960. Pile Driving Analysis by the Wave Equation. *Journal of the Soil Mechanics and Foundations Division* 86 (4): 35–61. doi:10.1061/TACEAT.0008470.

Sun, L., T. Jia, S. Yan, W. Guo, Y. Ren, and Z. Lei. 2016. Prediction of Pile Running during the Driving Process of Large Diameter Pipe Piles. *Ocean Engineering* 128: 48–57. doi:10.1016/j.oceaneng.2016.10.023.

Van Ravenzwaaij, J., M. Iten, R. Spruit, and A. De Boer. 2018. Geotechnical and Structural Applications of Fiber-Optic Sensing. In *High Tech Concrete: Where Technology and Engineering Meet*, 1287–1298. Cham: Springer International Publishing. doi:10.1007/978-3-319-59471-2_149.

Webb, G. T., P. J. Vardanega, N. A. Hoult, P. R. A. Fidler, P. J. Bennett, and C. R. Middleton. 2017. Analysis of Fiber-Optic Strain-Monitoring Data from a Prestressed Concrete Bridge. *Journal of Bridge Engineering* 22 (5): 05017002. doi:10.1061/(ASCE)BE.1943-5592.0000996.

Wu, W., Y. Wang, D. Tang, Q. Yue, Y. Du, Z. Fan, Y. Lin, and Y. Zhang. 2016. Design, Implementation and Analysis of Full Coupled Monitoring System of FPSO with Soft Yoke Mooring System. *Ocean Engineering* 113: 255–263. doi:10.1016/j.oceaneng.2015.12.035.

Yi, J. H. 2016. Laboratory Tests on Local Damage Detection for Jacket-Type Offshore Structures Using Optical FBG Sensors Based on Statistical Approaches. *Ocean Engineering* 124: 94–103. doi:10.1016/j.oceaneng.2016.07.060.

Zheng, X., B. Shi, H. H. Zhu, C. C. Zhang, X. Wang, and M. Sun. 2021. Performance Monitoring of Offshore PHC Pipe Pile Using BOFDA-Based Distributed Fiber Optic Sensing System. *Geomechanics and Engineering* 24: 337–348. doi:10.12989/gae.2021.24.4.337.

Zhu, H. H., B. Shi, and C. C. Zhang. 2017. FBG-Based Monitoring of Geohazards: Current Status and Trends. *Sensors* 17 (3): 452. doi:10.3390/s17030452.